Journal of
Materials Chemistry A

ROYAL SOCIETY
OF CHEMISTRY

PAPER

View Article Online
View Journal | View Issue

Open Access Article. Published on 16 April 2025. Downloaded on 2/4/2026 10:01:31 PM.
This article is licensed under a Creative Commons Attribution-NonCommercial 3.0 Unported Licence.

Check for updates

Cite this: *J. Mater. Chem. A*, 2025, **13**, 15941

Hierarchically structured superhydrophobic composite films for efficient radiative cooling and energy saving†

Ruiming Tan,[a] Hongbin Zhang,[a] Le Wang,[a] Yinyan Li,[a] Peng Xue,*[b] Shiqing Xu[a] and Gongxun Bai*[a]

Received 10th February 2025
Accepted 16th April 2025

DOI: 10.1039/d5ta01065a

rsc.li/materials-a

Passive daytime radiative cooling (PDRC) is a sustainable strategy for lowering surface temperatures by maximizing solar reflection and efficiently emitting thermal energy in the mid-infrared range. However, the effective application of PDRC materials is frequently constrained by performance deterioration caused by surface contamination in real-world environments. In this study, we present a high-performance composite film that integrates superhydrophobic self-cleaning properties, exceptional radiative cooling capabilities, and effective thermal insulation. The film features a hierarchical micro/nanostructure, composed of porous polydimethylsiloxane (PDMS), micron-sized glass microspheres, and nanoscale hydrophobic SiO_2 particles. This structural design enhances the solar reflectance and infrared emissivity by leveraging the multi-scale roughness and porosity. The film achieves an impressive solar reflectance of 94.2% and an infrared emissivity of 95.6%. Additionally, it exhibits a water contact angle of 160°, showcasing exceptional superhydrophobicity. This synergistic design enables a subambient temperature reduction of up to 7.8 °C under direct sunlight. Moreover, the superhydrophobic self-cleaning properties effectively prevent surface fouling and wetting, ensuring long-term operational stability and efficiency. These characteristics make the composite film a promising candidate for advanced thermal management in applications such as electronics, vehicles, and building materials.

1 Introduction

Heating and cooling systems account for approximately 48% of a building's energy consumption, making them the largest global energy consumers and significant contributors to greenhouse gas emissions and global warming.[1–3] The intensification of climate change and rising global temperatures have led to an ever-growing demand for electricity, further exacerbating environmental challenges.[4–6] Consequently, designing affordable and highly efficient cooling materials that can alleviate energy consumption and minimize climate impacts has emerged as a key area of research.[7–10] One of the most promising thermal management strategies is passive daytime radiative cooling (PDRC), which utilizes surfaces with high solar reflectance ($\bar{R}_{\text{solar}}$) and efficient longwave infrared emission ($\bar{\varepsilon}_{\text{LWIR}}$) within the atmospheric transparency window (8–13 μm).[11–14] This enables the surface to radiate heat into the outer space, where the temperature is approximately 3 K, creating a significant thermal differential with the Earth's surface temperature (around 288 K), thus achieving a cooling effect with zero energy consumption and zero emissions.[15–19]

In recent years, many studies have focused on the optical properties of materials, modifying and combining them to design radiative coolers with certain cooling performance. These designs include inorganic or metallic structures,[20] metal–polymer hybrid coatings[21,22] polymer-based composites,[23,24] porous materials,[18,25] and other advanced configurations. Despite significant progress, the practical application of PDRC materials remains constrained by limited weatherability under outdoor conditions.[26,27] Outdoor-exposed PDRC systems inevitably accumulate dust and contaminants, degrading the solar reflectance and cooling efficiency.[28,29] Current radiative cooling materials often exhibit hydrophobic or hydrophilic surface properties, making them prone to the accumulation of solid contaminants that impair solar reflectance and thermal infrared emissivity. These issues substantially degrade the overall cooling efficiency over time. Even hydrophobic materials face challenges under dynamic environmental conditions, such as exposure to rain or fluctuating humidity, which can lead to water accumulation and further diminish radiative cooling performance.[30,31]

---

[a] *Key Laboratory of Rare Earth Optoelectronic Materials and Devices of Zhejiang Province, China Jiliang University, Hangzhou 310018, China. E-mail: baigx@cjlu.edu.cn*

[b] *Beijing Key Laboratory of Green Building Environment and Energy Saving Technology, Beijing University of Technology, Beijing 100124, China. E-mail: xp@bjut.edu.cn*

† Electronic supplementary information (ESI) available. See DOI: https://doi.org/10.1039/d5ta01065a

Open Access Article. Published on 16 April 2025. Downloaded on 2/4/2026 10:01:31 PM.
This article is licensed under a Creative Commons Attribution-NonCommercial 3.0 Unported Licence.

To address these challenges, we developed a hierarchically structured superhydrophobic passive daytime radiative cooling (SDRC) film, offering efficient cooling, self-cleaning, and thermal insulation properties. This film combines high solar reflectance, strong mid-infrared emissivity, and exceptional environmental stability, making it a promising solution for practical applications. The SDRC film was fabricated using a composite of polydimethylsiloxane (PDMS), glass microspheres, and SiO_2 particles, processed through a phase separation technique. PDMS was chosen as the matrix material due to its high mid-infrared emissivity in the 8–13 μm atmospheric window, enabling efficient radiative heat dissipation. Additionally, the inherent hydrophobicity of PDMS contributes to the film's self-cleaning capabilities by repelling water and dirt. The flexibility and chemical stability of PDMS ensure long-term durability under various environmental conditions. The incorporation of glass microspheres into the PDMS matrix enhances thermal insulation and reduces solar absorption through Mie scattering. Meanwhile, nanoscale SiO_2 particles improve solar reflectance across the 0.3–2.5 μm spectrum while maintaining strong mid-infrared emission. The abundant Si–O functional groups in SiO_2 enhance the emissivity of the composite film by strengthening molecular vibrational modes within the atmospheric window. The combination of the nanoscale roughness of SiO_2 and the low surface energy of PDMS further enhances the film's superhydrophobicity, providing robust self-cleaning and anti-fouling properties. Furthermore, the mechanical flexibility and chemical stability of SDRC films make them suitable for diverse real-world applications. This work aims to demonstrate the potential of SDRC films as a promising solution for improving energy efficiency and sustainability in building cooling systems while addressing the critical issue of environmental durability in radiative cooling technologies.

2 Experimental section

2.1 Materials

PDMS was obtained from the Sylgard 184 silicone elastomer base, which contains the PDMS prepolymer A and curing agent B supplied by Dow Corning Co. Ethyl acetate was sourced from Shanghai Macklin Biochemical Co., Ltd, and titanium dioxide (TiO_2, AR, 99.9%) and hydrophobic silica were sourced from Aladdin Biochemical Technology Co., Ltd. Glass microspheres (∼14 μm) were acquired from 3M Company. All chemical reagents and samples were used as received, without any further treatment. Aluminum foil and polyethylene (PE) film were procured from local suppliers.

2.2 Preparation and optimization of superhydrophobic SDRC films

PDMS prepolymer A (5 g) and curing agent B (0.5 g) were added to 30 g of ethyl acetate, and the mixture was stirred magnetically at 25 °C for 1 hour to obtain a uniform solution. Water (2 g) was then introduced dropwise under high-speed stirring to induce phase separation, generating a semi-transparent sol. Subsequently, glass microspheres (1.786 g) and SiO_2 (0.356 g) were added under low-speed stirring to prevent particle fragmentation. The resulting sols were cast onto glass substrates of various sizes to achieve the desired sample thickness. After air-drying, the films were carefully peeled from the substrates, yielding self-supported SDRC films. The optimal composition was determined by testing different glass microsphere and SiO_2 ratios (Table S1†) based on reflectance (Fig. S1†) and emissivity (Fig. S2†). For comparison, a PDMS/TiO_2 film was fabricated with the same PDMS content as the SDRC film and TiO_2 content equivalent to the glass microsphere ratio in the SDRC film.

2.3 Characterization

The surface morphology of the materials was examined using a field emission scanning electron microscope (SEM, JEOL JSM-IT500, Japan), coupled with an energy dispersive X-ray spectrometer (EDS) to determine the elemental composition and distribution. The nanoparticle size distribution was analyzed using a nanoparticle size and zeta potential analyzer (Zetasizer Nano). The water contact angle of samples was analyzed using the DataPhysics OCA20 instrument. Reflectance spectra were measured at 0.2–2.5 μm using a UV-vis spectrophotometer (Shimadzu UV-3600). Employing the Nicolet iS50 analyzer, the transmittance (T), reflectance (R), and FTIR spectra of the sample were obtained by the integrated sphere test. The emissivity (E) was obtained from the formula $E = 1 - R - T$.

The solar reflectance ($\bar{R}_{\text{solar}}$) is defined by the following equation:

$$\overline{R}_{\text{solar}} = \frac{\int_{0.3}^{2.5} I_{\text{AM1.5}}(\lambda) \times R_{\text{solar}}(\lambda, \theta)\mathrm{d}\lambda}{\int_{0.3}^{2.5} I_{\text{AM1.5}}(\lambda)\mathrm{d}\lambda} \tag{1}$$

Here λ is the wavelength, θ is the incident angle, $I_{\text{AM1.5}}$ (λ) is the AM1.5 global standard solar spectrum, and R_{solar} (λ,θ) is the angular spectral reflectance of the surface.

The longwave infrared ($\bar{\varepsilon}_{\text{LWIR}}$) emission within the atmospheric transparency window (8–13 μm) is defined by the following equation:

$$\bar{\varepsilon}_{\text{LWIR}} = \frac{\int_{8}^{13} I_{\text{bb}}(T, \lambda) \times E(T, \lambda)}{\int_{8}^{13} I_{\text{bb}}(T, \lambda)} \tag{2}$$

where $I_{\text{bb}}(T,\lambda)$ is the emittance spectra of a blackbody at a temperature of T (here, T was assumed to be 25 °C) and $E(T,\lambda)$ is the spectral hemispherical thermal emittance of the surface.

3 Results and discussion

3.1 Schematic overview and design of the SDRC film with multifunctional properties and its fabrication

As depicted in Fig. 1a, the SDRC film reflects sunlight in the range of 0.3 to 2.5 μm while emitting thermal energy into the outer space through the atmospheric transparency window. Simultaneously, it prevents thermal conduction from the surrounding warmer environment, enabling passive sub-ambient radiative cooling during the day. Traditional roofing systems absorb heat, leading to increased indoor temperatures. In contrast, the SDRC film, as shown in Fig. 1b, provides radiative cooling, effectively maintaining indoor comfort and

Open Access Article. Published on 16 April 2025. Downloaded on 2/4/2026 10:01:31 PM.
This article is licensed under a Creative Commons Attribution-NonCommercial 3.0 Unported Licence.

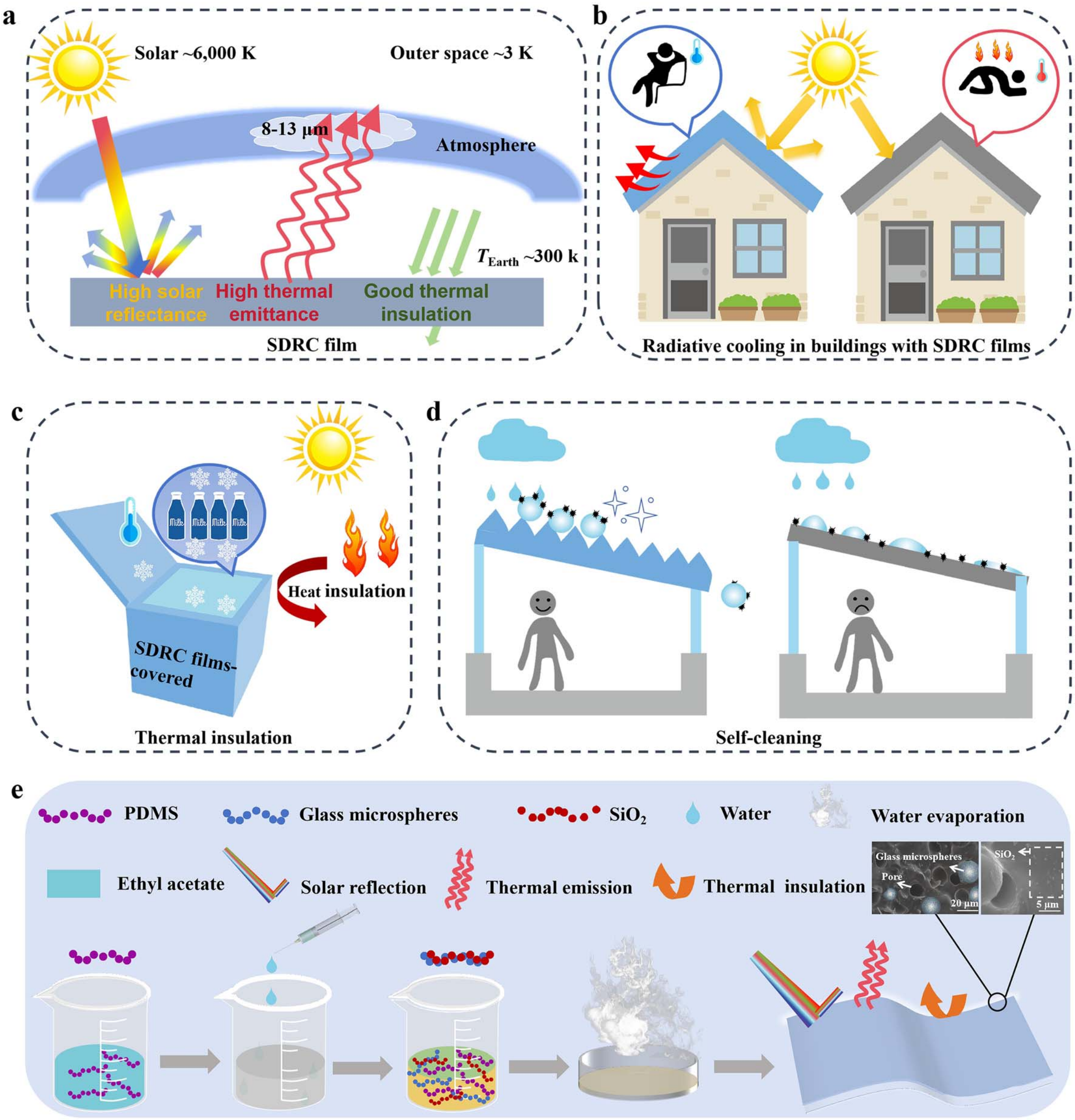

Fig. 1 Schematic illustration and design of the SDRC film with multifunctional properties and its fabrication. (a) Working principle of the SDRC film. (b) Application of SDRC as a roofing material for building energy savings. (c) Thermal insulation performance of the SDRC film, demonstrating its heat resistance. (d) Superhydrophobic self-cleaning properties of the SDRC film. (e) Illustration of the SDRC film fabrication process using a phase-separation method, with the inset showing an SEM image of the film. Blue circle markers highlight the glass microspheres in the SEM images.

contributing to building energy savings by reducing the need for active cooling. Fig. 1c demonstrates its application in thermal insulation, minimizing heat transfer from external sources. Fig. 1d highlights its superhydrophobic self-cleaning properties, ensuring long-term weatherability and stability. The fabrication process of the SDRC films utilizes a simple phase-separation method, as illustrated in Fig. 1e. During the evaporation of water and ethyl acetate, the film develops a micro/nano-structured surface, incorporating glass microspheres and hydrophobic SiO$_2$ particles (Fig. S3a†). This results in a hierarchical structure with well-defined porous features that contribute to both the thermal insulation and radiative cooling properties of the film. The presence of micro-sized glass microspheres (Fig. S3b†) and nano-sized SiO$_2$ particles (Fig. S3c†) creates a multi-scale roughness, enhancing the overall performance by enabling high solar reflectance and infrared emissivity.

3.2 Optical property testing of SDRC films

In order to determine the performance of the films, a series of characterization measurements were performed. Fig. 2a illustrates the reflectance spectrum of the SDRC film in both the solar and mid-infrared regions. The SDRC films exhibit an average $\bar{R}_{solar}$ of up to 94.2%, minimizing heat absorption from

Open Access Article. Published on 16 April 2025. Downloaded on 2/4/2026 10:01:31 PM.
This article is licensed under a Creative Commons Attribution-NonCommercial 3.0 Unported Licence.

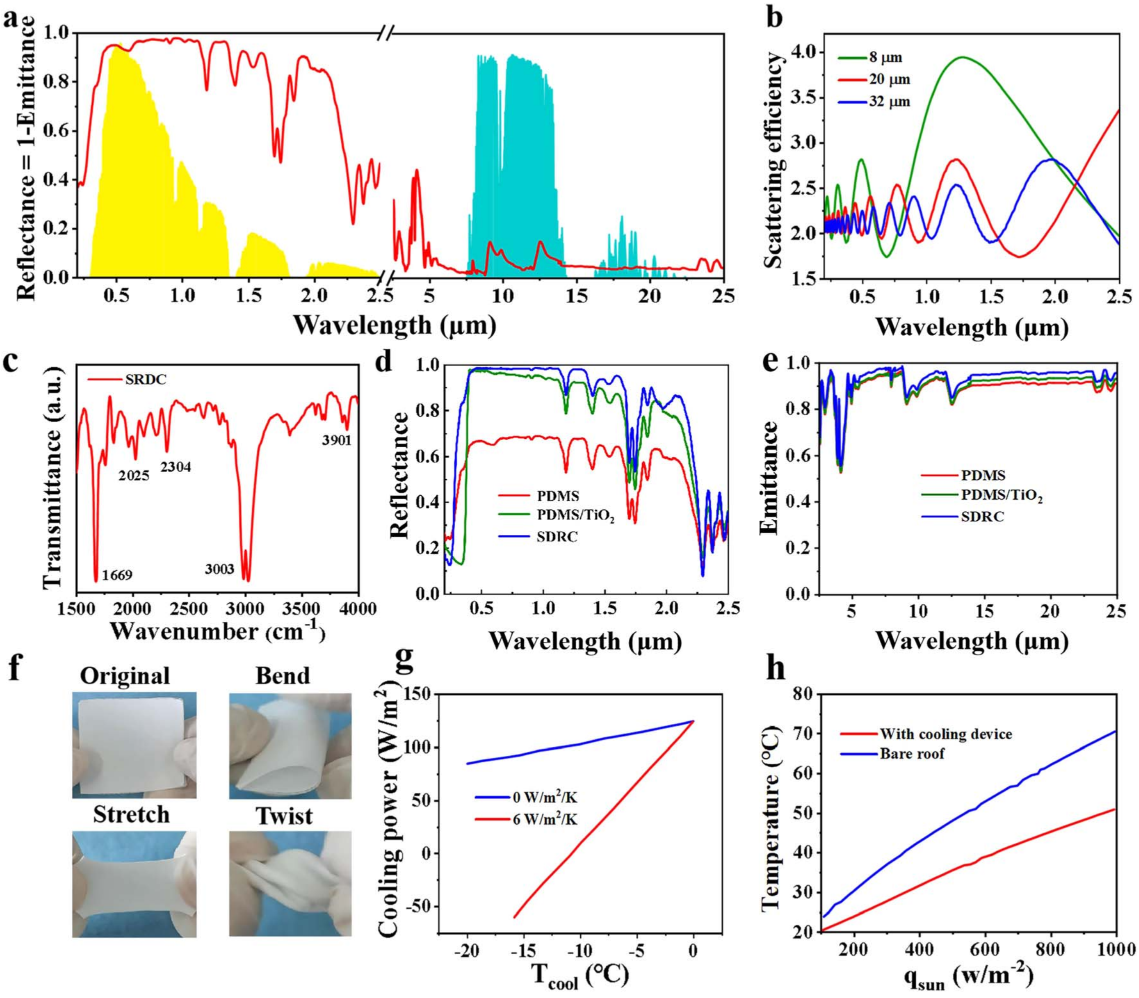

Fig. 2 Optical characteristics of SDRC films. (a) Reflectance of the SDRC film in the AM1.5 global solar spectrum (yellow) and in the atmospheric transparent spectral (cyan) background. (b) Simulated scattering efficiency of glass microspheres of varying sizes. (c) The FTIR spectra of SDRC film. (d) The reflectance spectra of the pure PDMS, PDMS/TiO$_2$, and SDRC films. (e) The emissivity spectra of pure PDMS, PDMS/TiO$_2$, and SDRC films. (f) Images of the SDRC film under different deformations, demonstrating its excellent mechanical resilience and flexibility. (g) The net cooling power was calculated using MATLAB software based on theoretical simulations. (h) The calculation of surface temperature comparisons at different solar radiation intensities.

the Sun.[32] Additionally, the films show a high $\bar{\varepsilon}_{\mathrm{LWIR}}$ greater than 95%, optimizing thermal emission within the atmospheric transparency window. Based on SEM testing of glass microspheres, the particle size distribution was obtained (Fig. S4†). The glass microspheres exhibit a particle size distribution ranging from 8 to 32 μm, with a distribution center located at approximately 14 μm. As shown in Fig. 2b, the distribution of glass microspheres of varying sizes contributes to enhancement of the scattering efficiency across the entire solar spectrum.[33] Moreover, Fig. 2c presents the FTIR spectrum of the SDRC film, highlighting absorption peaks at 1669 cm^{-1} and 3003 cm^{-1}, which are attributed to the C–Si and Si–O bonds, respectively.

To elucidate the contributions of individual components, FTIR spectra of PDMS, glass microspheres, and SiO$_2$ were analyzed. The FTIR spectrum of PDMS (Fig. S5a†) exhibits characteristic absorption peaks at 1257.32 cm^{-1}, 1010.04 cm^{-1}, and 787.78 cm^{-1}, corresponding to Si–CH$_3$ symmetric bending, Si–O–Si stretching, and Si–C rocking vibrations, respectively. Notably, the Si–O–Si stretching mode enhances the intrinsic mid-infrared emissivity of the PDMS matrix. The glass microspheres (Fig. S5b†) exhibit distinct Si–O vibrational absorptions at 1119.36 cm^{-1}, 1000.39 cm^{-1}, 846.60 cm^{-1}, and 539.01 cm^{-1}, which are characteristic of silicate structures. The peaks at 1119.36 cm^{-1} and 1000.39 cm^{-1} correspond to Si–O–Si symmetric and asymmetric stretching vibrations, respectively, indicating a well-structured silicate network. The absorption at 846.60 cm^{-1} is associated with Si–O bending vibrations or possible Si–OH stretching, while the 539.01 cm^{-1} peak corresponds to Si–O–Si bending modes within the silica framework. Notably, the broad absorption near 1000.39 cm^{-1} falls within the 8–13 μm atmospheric transparency window, which contributes to radiative cooling by effectively emitting thermal radiation in this range. The presence of Si in the glass microspheres is further confirmed by EDS analysis (Fig. S5c†).

Open Access Article. Published on 16 April 2025. Downloaded on 2/4/2026 10:01:31 PM.
This article is licensed under a Creative Commons Attribution-NonCommercial 3.0 Unported Licence.

Meanwhile, SiO_2 exhibits Si–O vibrations at 809.47 cm^{-1}, 457.53 cm^{-1}, and 1067.89 cm^{-1}, with the 1067.89 cm^{-1} stretching mode strongly interacting with thermal radiation (Fig. S5d†). The synergistic contributions of PDMS, glass microspheres, and SiO_2 significantly enhance the mid-infrared emissivity of the SDRC films, optimizing their radiative cooling performance.

Fig. 2d presents the reflectance spectra of pure PDMS, PDMS/TiO_2 composite, and SDRC films. The SDRC films exhibit the highest reflectance (~94.2%), surpassing commercial-grade TiO_2 due to the incorporation of glass microspheres and SiO_2. This enhancement is attributed to the hierarchical micro/nano structure,[34] which introduces a refractive index contrast between PDMS and air within the pores, amplifying Mie scattering and reducing solar absorption.[24] Pore size analysis revealed an average diameter of 13.58 μm with a standard deviation (SD) of 1.82 μm, and a distribution range of 11.76 μm to 15.40 μm (Fig. S6†). This porous structure further enhances solar reflectance by increasing light scattering and prolonging optical paths. Additionally, the nano-sized SiO_2 particles (~29.5 nm, Fig. S7†) enhance reflectance by amplifying Mie scattering, especially for visible light, reducing solar absorption. Fig. 2e shows that the SDRC films have the highest emissivity (~95.6%), indicating that the additional Si–O bonds introduced by the glass microspheres and SiO_2 enhance the film's emissivity in the mid-infrared range. In addition to material composition and microstructure, film thickness also plays a crucial role in optimizing the reflectance and emissivity. Reflectance measurements indicate that increasing the thickness initially improved the solar reflectance, but beyond 580 μm, further gains were negligible (Fig. S8a†). Similarly, emissivity remained stable across all tested thicknesses (Fig. S8b†). Therefore, 580 μm was identified as the optimal thickness, balancing high solar reflectance and efficient thermal insulation while minimizing material weight. Notably, the SDRC film displays impressive mechanical durability and flexibility. As illustrated in Fig. 2f, the film completely recovers to its initial shape after multiple deformations, showing no signs of cracking or structural failure when pressure is released. Specifically, the cyclic compressive stress–strain curves (Fig. S9a†) highlight the film's excellent compressibility and low elastic modulus, making it well-suited for deployment on curved surfaces in practical scenarios. Fig. S9b and S9c† show the results of cyclic testing, where the elasticity of the films remained largely unchanged after multiple stretches, further demonstrating their robust mechanical properties. In addition, the relationship between cooling power and the heat transfer coefficient (h) with the environment was studied. As shown in Fig. 2g, when the surface temperature (T_{sur}) of the SDRC film is lower than the ambient temperature (T_{amb}) (*i.e.*, $T_{\text{cool}} = T_{\text{sur}} - T_{\text{amb}} < 0$), its cooling power decreases with an increase in h (*e.g.*, from $h = 0$ to $h = 6$). When the T_{sur} of the SDRC film matches the T_{amb} (*i.e.*, $T_{\text{cool}} = 0$), the net cooling efficiency is unaffected by h, and the two lines converge at the same point. Additionally, we analyzed the film's surface temperature under different solar irradiance levels. As shown in Fig. 2h, the roof covered with the SDRC film achieves better cooling performance compared to a roof directly exposed to air.

3.3 Indoor/outdoor thermal management testing of SDRC films

To validate the cooling capability of the SDRC film under real-world conditions, we constructed an experimental device. The experimental device, designed to minimize thermal convection and radiation interference from the surrounding environment, is schematically shown in Fig. 3a. It was constructed using solar- and infrared-transparent polyethylene (PE) for shielding, and the sides were enclosed with highly reflective aluminum foil. The outdoor model used for the experiments is shown in Fig. 3b. Indoor cooling tests were initially performed with a high-intensity xenon lamp to simulate solar radiation, ensuring a uniform power distribution of 1000 W m^{-2} on the sample surface. When the lamp was turned on, the temperature of the air shielded by the PE film rapidly increased from 25 °C to 45.2 °C (see Fig. 3c), eventually stabilizing at 46.3 °C. However, the interior temperature of the SDRC film remained at only 38.5 °C, significantly lower than the temperature of the PE film shielded air, demonstrating the film's superior cooling capability. The temperature difference (ΔT) between the SDRC film and the PE shielding air was found to be 7.3 °C on average, with a peak value of 7.8 °C. In contrast, the PDMS/TiO_2 film only exhibited a ΔT of 3.5 °C. The significant ΔT can primarily be attributed to the SDRC film's higher solar reflectance, which effectively reduces the absorption of a substantial amount of visible light.

In addition, we conducted outdoor thermal testing to evaluate the cooling performance of the SDRC. In Fig. 3d–f, the internal temperature beneath the SDRC film was 7.8 °C lower than that of the air shielded by the PE film under an average solar intensity (I_{solar}) of 859 W m^{-2}. Notably, at peak solar intensity, the temperature decrease reached as high as 13.9 °C, accompanied by a midday humidity level of 17%. In contrast, the average temperature drop for the PDMS/TiO_2 film was merely 3.4 °C, with a peak of 4.5 °C observed during the same duration (Fig. 3e). These excellent cooling performances of SDRC films can be attributed to three key factors: (a) the hierarchical micro/nanoporous structure enhances the overall solar reflectance. (b) The films exhibit high thermal emissivity, promoting efficient heat radiation. (c) The glass microspheres, which contain air within their structure, have a low thermal conductivity, effectively insulating against heat and further improving the cooling performance.

Moreover, under certain cooling performance requirements, its superhydrophobicity is also an important performance indicator. Fig. 3g shows the image of water droplets rolling over the SDRC film, which also proves that the film has superhydrophobic properties. Fig. S10a† shows that the superhydrophobicity allows a variety of droplets, such as dyed water, to take on a near-spherical shape on the film, exhibiting excellent liquid-repelling properties. Fig. S10b† displays the water contact angle of the SDRC film, revealing its exceptional superhydrophobic characteristics with an angle of

Open Access Article. Published on 16 April 2025. Downloaded on 2/4/2026 10:01:31 PM.
This article is licensed under a Creative Commons Attribution-NonCommercial 3.0 Unported Licence.

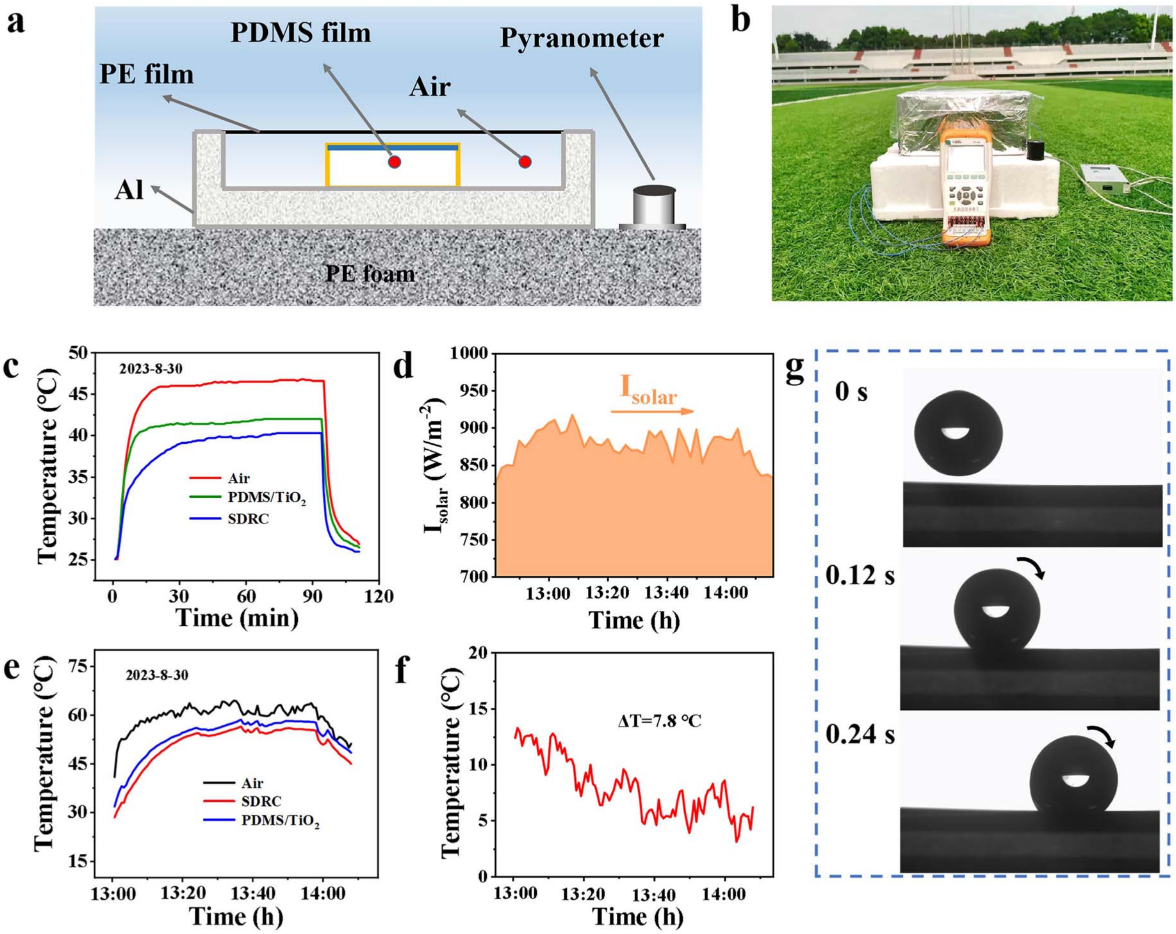

Fig. 3 Characterization of superhydrophobic characteristics and outdoor cooling performance of SDRC films. (a) The schematics of the self-made experimental setup. (b) The digital image of the experimental setup placed on a grassy area. (c) Temperature variations of the surrounding air (red line), PDMS/TiO_2 film (green line), and SDRC film (dark blue line) under xenon lamp exposure, simulating solar irradiation of approximately 1000 W m^{-2}. (d) Real-time measurements of solar intensity and the corresponding temperatures for each component of experimental setup during the testing. (e) Internal temperature beneath the sample cover. (f) Comparison of the internal air temperature differences beneath the SDRC film cover and the PE film cover. (g) The contact angle images of a water droplet rolling over the SDRC film.

approximately 160°. This distinctive property provides the film with self-cleaning capability, as shown in Fig. S11.† The water droplets effortlessly roll off the surface, carrying away any dirt, thus maintaining the film's cleanliness. Additionally, the SDRC film prevents the accumulation of muddy water, as the droplets do not adhere to the surface, keeping it pristine even after exposure to contaminants.

3.4 Outdoor thermal imaging testing

The thermal effects resulting from the high infrared reflectivity of high emissivity films can be visualized by a thermal imaging camera. We selected SDRC films as model samples for comparison with PDMS/TiO_2 films. Initially, two identical plastic plates were positioned on separate spots of a shared heating surface, as illustrated in Fig. S12a.† One is covered by our SDRC high emissivity film, while the other is covered with a PDMS/TiO_2 film. Their surfaces appear similar (top row, Fig. S12b†), but after temperature stabilization, the thermal images reveal significant differences (bottom row, Fig. S12b†). The PDMS/TiO_2 film exhibits a higher surface temperature under the thermal camera, whereas the SDRC film, with its lower surface temperature, demonstrates reduced thermal radiation.

The excellent cooling properties of SDRC films were further evaluated by cooling an object in direct sunlight. The thermal infrared images reveal that the temperature of the exposed black seat reaches 60.8 °C, while the region covered by the SDRC film maintains a significantly lower temperature of 32.6 °C (Fig. 4a). As shown in Fig. 4b and c, the film achieved an average temperature reduction of 24.4 °C, under conditions with a maximum ambient temperature of 37 °C and an average solar intensity of 804.1 W m^{-2}. Similarly, in Fig. 4d, SDRC was applied to simulate the car's outer shell. After one hour of exposure, the surface temperature was captured using an infrared thermal imaging camera. The thermal image and the corresponding temperature values are displayed on the right side of Fig. 4d. The surface temperature of the uncovered car reached 48.2 °C, while the SDRC-covered surface remained at 34.2 °C, demonstrating a temperature difference of 14 °C.

Open Access Article. Published on 16 April 2025. Downloaded on 2/4/2026 10:01:31 PM.
This article is licensed under a Creative Commons Attribution-NonCommercial 3.0 Unported Licence.

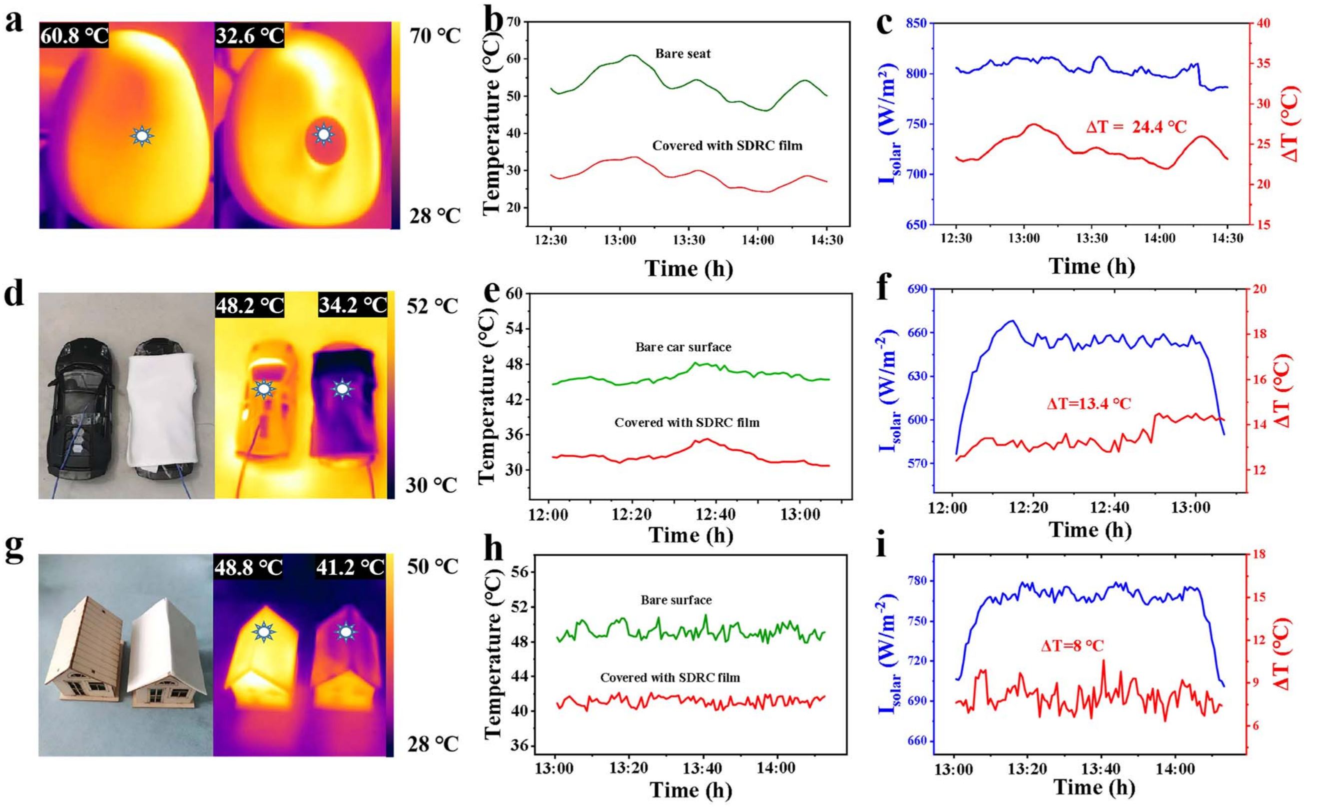

Fig. 4 SDRC film for outdoor cooling applications. (a) Thermal infrared images of two identical black seats, with the left seat exposed to sunlight and the right seat partially covered with the SDRC film. (b) Recorded real-time temperatures of the bare black seat and the black seat covered with the SDRC film. (c) The Δ*T* between the bare black seat and the black seat covered with the SDRC film (ambient temperature is 37 °C). (d) Thermal infrared and visible images comparing two identical cars, one covered with the SDRC film and the other uncovered. (e) Recorded interior temperatures of the two cars under different conditions: one uncovered and the other covered with the SDRC film. (f) The interior Δ*T* between the temperature of the bare car model and the car model covered with the SDRC film. (g) Thermal infrared and optical images of two identical house models, one featuring an SDRC film cover and the other bare. (h) Recorded interior temperatures of the two house models under different conditions: one uncovered and the other covered with the SDRC film. (i) The interior Δ*T* between the bare house and the house model covered with the SDRC film.

Additionally, a temperature sensor was employed to monitor the real-time interior temperature of the car, as shown in Fig. 4e. The calculated temperature differences are presented in Fig. 4f, with the average temperature difference between the two conditions reaching 13.4 °C. To demonstrate the potential of the SDRC film for building applications, we selected a simplified building model as the test subject (Fig. 4g). Using a similar testing approach, the surface temperature of the SDRC film, as captured by thermal imaging, was 41.2 °C, while the surface temperature of the uncovered building model reached 48.8 °C, resulting in a temperature difference of 7.6 °C. Additionally, the internal temperature changes over one hour are shown (Fig. 4h), with an average temperature difference of 8 °C observed during the testing period, as illustrated in Fig. 4i. These findings highlight the remarkable cooling performance of SDRC films, which hold great potential for reducing energy consumption in outdoor cooling applications.

3.5 Weathering and stability testing of the SDRC films

For real-world applications, it is crucial that the film maintains its stability and performance even when exposed to challenging environmental conditions.[35] We have also evaluated the feasibility of the SDRC film as a cooling material in production and life through acid and alkaline tests, and high and low temperature tests. In the acid and alkaline durability test, the changes in the mass of the SDRC film were examined when exposed to acidic and alkaline conditions. As illustrated in Fig. 5a, after 5 days of immersion in dilute hydrochloric acid (pH = 2), the film showed an almost negligible mass loss, from 0.515 g to 0.514 g, indicating its excellent stability in acidic environments. In a similar test, the film was exposed to a sodium carbonate solution (pH = 10) for 5 days, further confirming its durability under alkaline conditions. The quality of the SDRC film remained essentially unchanged after immersion, indicating that the SDRC film also has excellent resistance to alkaline environments.

Since the temperature in the environment changes all the time, we simulated a high and a low temperature environment to test its effect on SDRC films. As shown in Fig. 5b, the SDRC films were subjected to relatively high (200 °C) and low (−30 °C) temperatures for 48 hours to evaluate their thermal stability. After exposure to low temperatures, the films were dried in a 50 °C oven for 5 hours before measuring their mass. The results

Open Access Article. Published on 16 April 2025. Downloaded on 2/4/2026 10:01:31 PM.
This article is licensed under a Creative Commons Attribution-NonCommercial 3.0 Unported Licence.

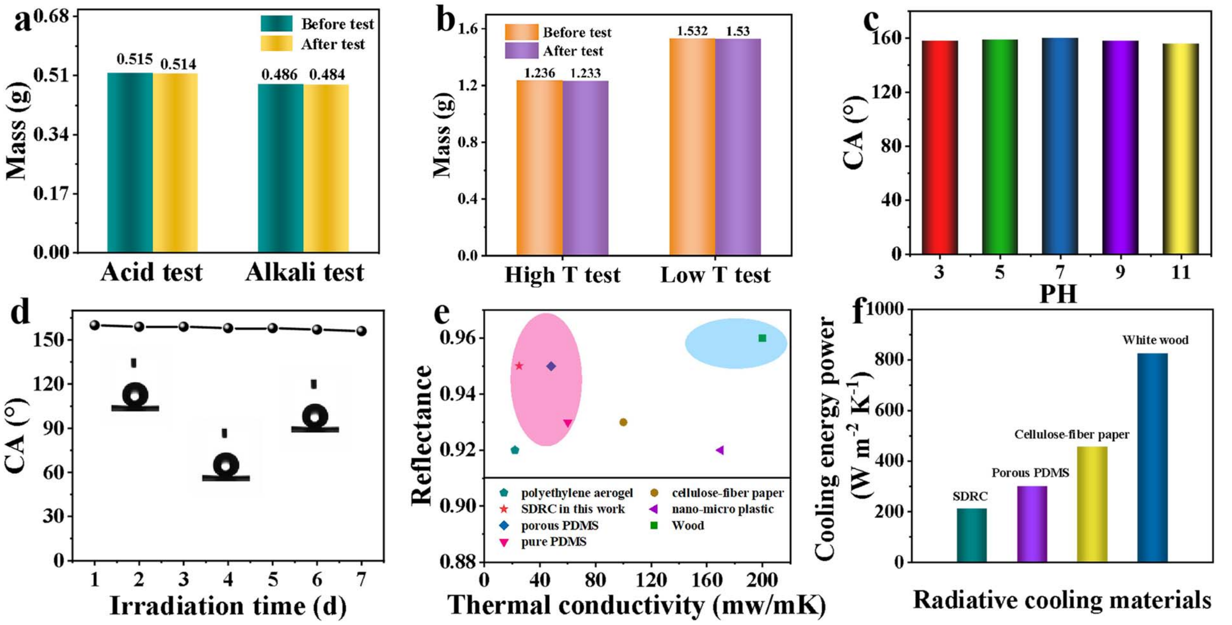

Fig. 5 Chemical durability testing of SDRC films. (a) Recorded changes in the quality of SDRC films after immersion in acid and alkali solutions for 120 hours. (b) Recorded quality changes of SDRC films after high and low temperature treatments. (c) The measured CA values of SDRC films after being immersed in various pH solutions for 120 hours. (d) The change in the CA of superhydrophobic surfaces over time under UV exposure. (e) A comparative analysis of the thermal conductivity and solar reflectance characteristics of SDRC films in relation to other radiative cooling materials reported in prior studies. (f) Comparison of the simulated cooling energy consumption for various typical radiative cooling materials.

showed negligible changes, confirming the excellent resistance of SDRC films to extreme temperatures and their suitability for diverse applications. To assess the stability of the superhydrophobic properties of SDRC films, we conducted tests on their chemical durability and UV resistance. The films were subjected to exposure to various pH solutions and UV irradiation over an extended period. Initially, the samples were submerged in solutions ranging from pH 1 to 14 for 120 hours, after which they were thoroughly rinsed and dried at 40 °C. After this treatment, the contact angle (CA) of the films remained above 150°, demonstrating their exceptional resistance to both acidic and alkaline conditions, as depicted in Fig. 5c. The remarkable stability of SDRC films to chemical corrosion can be attributed to the air cushion layer formed between the solution and the superhydrophobic surface, which acts as a protective barrier, preventing direct contact between the film and the acid or alkaline solutions. This layer effectively shields the films from degradation, demonstrating their strong resistance to chemical corrosion. In addition, the UV stability of the films was also evaluated. The results revealed that the CA of the SDRC films exhibited minimal changes after UV exposure (Fig. 5d).

Furthermore, after undergoing a series of mechanical deformation tests, including bending, stretching, and twisting, the reflectance (Fig. S13a†) and emissivity (Fig. S13b†) of the SDRC films remained stable. The water contact angle measurements confirmed that the films retained their superhydrophobicity (Fig. S13c†), while mass analysis showed no detectable material loss (Fig. S13d†). These results indicate that the surface structure remained intact without significant detachment of SiO_2 nanoparticles or glass microspheres, further demonstrating excellent mechanical and structural stability of the SDRC films. Moreover, SDRC films exposed outdoors for 10 days were sealed and stored for over three months. Reflectance (Fig. S14a†) slightly decreased due to dust adhesion and minor structural changes, while emissivity (Fig. S14b†) remained nearly unchanged since the SiO_2 and glass microsphere structures remained intact, demonstrating excellent durability and stability. A comparison of the thermal conductivity and solar reflectance properties of SDRC films with other porous radiative cooling materials was conducted, as shown in Fig. 5e. Its thermal conductivity is relatively low, measured at 31 $mW\ m^{-1}\ K^{-1}$, which can be attributed to the glass microspheres. These microspheres are hollow, allowing them to significantly enhance thermal insulation by trapping air inside. As presented in Fig. 5f, the SDRC films exhibit exceptionally low cooling energy consumption, measured at 213 $W\ m^{-2}\ K^{-1}$. This makes SDRC films significantly more energy-efficient than other materials, such as porous PVDF films, cellulose-fiber paper, and white wood, with the cooling energy consumption of white wood reaching as high as 825 $W\ m^{-2}\ K^{-1}$. This further emphasizes the superior cooling performance and energy-saving capability of the SDRC films.

4 Conclusion

In summary, we introduce a phase separation approach to develop porous superhydrophobic composite polymer films with micro/nanoscale structures that integrate self-cleaning, thermal insulation and radiative cooling properties. With the combination of glass microspheres, silica, and micro/

Open Access Article. Published on 16 April 2025. Downloaded on 2/4/2026 10:01:31 PM.
This article is licensed under a Creative Commons Attribution-NonCommercial 3.0 Unported Licence.

nanoporous structures, the SDRC film achieves a solar reflectance of 94.2%. Additionally, the polymer's functional groups and the Si–O bonds introduced by the particles contribute to a high mid-infrared emissivity of 95.6%. Furthermore, under an outdoor solar intensity of ~859 W m^{-2}, the SDRC film achieved an average sub-environmental cooling of approximately 7.8 °C, with a maximum temperature difference reaching 13.9 °C. Notably, the SDRC film exhibits superhydrophobic self-cleaning properties, with a water contact angle of 160°, and has passed extensive durability and stability tests, maintaining long-term self-cleaning effectiveness. This contributes to the sustained cooling performance of the film, ensuring its reliability in real-world outdoor environments. This work proposes an effective strategy that combines self-cleaning, thermal insulation, and radiative cooling with great potential for applications in sustainable, energy-saving ways.

Data availability

The data supporting this article have been included as part of the ESI.†

Author contributions

Ruiming Tan: conceptualization, investigation, methodology, software, writing – original draft, writing – review & editing. Hongbin Zhang: methodology, writing – review & editing. Le Wang: writing – review & editing, visualization. Yinyan Li: writing – review & editing. Peng Xue: supervision, writing – review & editing. Shiqing Xu: supervision, writing – review & editing. Gongxun Bai: conceptualization, funding acquisition, supervision, writing – review & editing.

Conflicts of interest

There are no conflicts to declare.

Acknowledgements

Financial support from the National Key Research and Development Project of China (2021YFB3502100), and Zhejiang Provincial Natural Science Foundation of China (LR24F050002) is gratefully acknowledged.

References

1 R. H. Wu, C. X. Sui, T. H. Chen, Z. R. Zhou, Q. Z. Li, G. B. Yan, Y. Han, J. W. Liang, P. J. Hung, E. Luo, D. V. Talapin and P. C. Hsu, *Science*, 2024, **384**, 1203–1212.

2 F. Xie, W. Jin, J. R. Nolen, H. Pan, N. Yi, Y. An, Z. Zhang, X. Kong, F. Zhu, K. Jiang, S. Tian, T. Liu, X. Sun, L. Li, D. Li, Y.-F. Xiao, A. Alu, S. Fan and W. Li, *Science*, 2024, **386**, 788–794.

3 M. L. Qin, K. H. Jia, A. Usman, S. H. Han, F. Xiong, H. W. Han, Y. K. Jin, W. Aftab, X. Y. Geng, B. B. Ma, Z. Ashraf, S. Gao, Y. G. Wang, Z. H. Shen and R. Q. Zou, *Adv. Mater.*, 2024, **36**, 10.

4 X. Z. Zhao, J. C. Li, K. C. Dong and J. Q. Wu, *ACS Nano*, 2024, **18**, 18118–18128.

5 H. J. Tang, C. Y. Guo, F. Fan, H. D. Pan, Q. H. Xu and D. L. Zhao, *Energy Environ. Sci.*, 2024, **17**, 11.

6 J. R. Liu, Y. Q. Wei, Y. Zhong, L. P. Zhang, B. J. Wang, X. L. Feng, H. Xu and Z. P. Mao, *Adv. Funct. Mater.*, 2024, **34**, 14.

7 D. Li, X. Liu, W. Li, Z. H. Lin, B. Zhu, Z. Z. Li, J. L. Li, B. Li, S. H. Fan, J. W. Xie and J. Zhu, *Nat. Nanotechnol.*, 2021, **16**, 153.

8 J. L. Li, Y. Liang, W. Li, N. Xu, B. Zhu, Z. Wu, X. Y. Wang, S. H. Fan, M. H. Wang and J. Zhu, *Sci. Adv.*, 2022, **8**, 8.

9 P. L. Li, A. Wang, J. J. Fan, Q. Kang, P. K. Jiang, H. Bao and X. Y. Huang, *Adv. Funct. Mater.*, 2022, **32**, 10.

10 J. W. Ma, F. R. Zeng, X. C. Lin, Y. Q. Wang, Y. H. Ma, X. X. Jia, J. C. Zhang, B. W. Liu, Y. Z. Wang and H. B. Zhao, *Science*, 2024, **385**, 68–74.

11 J. Mandal, Y. Yang, N. F. Yu and A. P. Raman, *Joule*, 2020, **4**, 1350–1356.

12 Z. W. Shao, A. B. Huang, C. C. Cao, X. W. Ji, W. Hu, H. J. Luo, J. Bell, P. Jin, R. G. Yang and X. Cao, *Nat. Sustain.*, 2024, **7**, 11.

13 Y. P. Tian, X. J. Liu, Z. Q. Wang, J. S. Li, Y. Mu, S. Y. Zhou, F. Q. Chen, M. L. Minus, G. Xiao and Y. Zheng, *Nano Energy*, 2022, **96**, 10.

14 Z. Y. Wang, J. R. Liang, D. Y. Lei, C. C. Jiang, Z. Yang, G. X. Yang, D. Q. Zhang, L. X. Zhang, C. Y. Zhang and Y. F. Bai, *Appl. Energy*, 2024, **369**, 8.

15 X. K. Wu, J. L. Li, F. Xie, X. E. Wu, S. M. Zhao, Q. Y. Jiang, S. L. Zhang, B. S. Wang, Y. R. Li, D. Gao, R. Li, F. Wang, Y. Huang, Y. L. Zhao, Y. Y. Zhang, W. Li, J. Zhu and R. F. Zhang, *Nat. Commun.*, 2024, **15**, 11.

16 X. B. Yin, R. G. Yang, G. Tan and S. H. Fan, *Science*, 2020, **370**, 786.

17 D. L. Zhao, A. Aili, Y. Zhai, J. T. Lu, D. Kidd, G. Tan, X. B. Yin and R. G. Yang, *Joule*, 2019, **3**, 111–123.

18 J. Y. Zhao, Q. Meng, Y. Li, Z. C. Yang and J. T. Li, *ACS Appl. Mater. Interfaces*, 2023, **15**, 47286–47293.

19 Y. W. Zhao, D. Pang, M. J. Chen, Z. Chen and H. J. Yan, *Appl. Mater. Today*, 2022, **26**, 8.

20 H. W. Zhang, K. C. S. Ly, X. H. Liu, Z. H. Chen, M. Yan, Z. L. Wu, X. Wang, Y. B. Zheng, H. Zhou and T. X. Fan, *Proc. Natl. Acad. Sci. U. S. A.*, 2020, **117**, 14657–14666.

21 Y. Zhou, H. M. Song, J. W. Liang, M. Singer, M. Zhou, E. Stegenburgs, N. Zhang, C. Xu, T. Ng, Z. F. Yu, B. Ooi and Q. Q. Gan, *Nat. Sustain.*, 2019, **2**, 718–724.

22 Z. B. Yang, Y. Jia and J. Zhang, *ACS Appl. Mater. Interfaces*, 2022, **14**, 24755–24765.

23 S. Y. Jeong, C. Y. Tso, Y. M. Wong, C. Y. H. Chao and B. Huang, *Sol. Energy Mater. Sol. Cells*, 2020, **206**, 10.

24 M. C. Huang, C. H. Xue, J. Y. Huang, B. Y. Liu, X. J. Guo, Z. X. Bai, R. X. Wei, H. D. Wang, M. M. Du, S. T. Jia, Z. Chen and Y. K. Lai, *Chem. Eng. J.*, 2022, **442**, 11.

25 Y. Liu, A. Caratenuto, F. Q. Chen and Y. Zheng, *Chem. Eng. J.*, 2024, **488**, 11.

26 X. H. Liu, C. Y. Xiao, P. Wang, M. Yan, H. F. Wang, P. W. Xie, G. Liu, H. Zhou, D. Zhang and T. X. Fan, *Adv. Opt. Mater.*, 2021, **9**, 10.

Open Access Article. Published on 16 April 2025. Downloaded on 2/4/2026 10:01:31 PM.
This article is licensed under a Creative Commons Attribution-NonCommercial 3.0 Unported Licence.

27 J. Mandal, Y. K. Fu, A. C. Overvig, M. X. Jia, K. R. Sun, N. N. Shi, H. Zhou, X. H. Xiao, N. F. Yu and Y. Yang, *Science*, 2018, **362**, 315–318.

28 S. N. Zeng, S. J. Pian, M. Y. Su, Z. N. Wang, M. Q. Wu, X. H. Liu, M. Y. Chen, Y. Z. Xiang, J. W. Wu, M. N. Zhang, Q. Q. Cen, Y. W. Tang, X. H. Zhou, Z. H. Huang, R. Wang, A. Tunuhe, X. Y. Sun, Z. G. Xia, M. W. Tian, M. Chen, X. Ma, L. Yang, J. Zhou, H. M. Zhou, Q. Yang, X. Li, Y. G. Ma and G. M. Tao, *Science*, 2021, **373**, 692.

29 E. Rephaeli, A. Raman and S. H. Fan, *Nano Lett.*, 2013, **13**, 1457–1461.

30 A. P. Raman, M. Abou Anoma, L. X. Zhu, E. Rephaeli and S. H. Fan, *Nature*, 2014, **515**, 540.

31 N. N. Shi, C. C. Tsai, M. J. Carter, J. Mandal, A. C. Overvig, M. Y. Sfeir, M. Lu, C. L. Craig, G. D. Bernard, Y. Yang and N. F. Yu, *Light:Sci. Appl.*, 2018, **7**, 9.

32 K. C. Tang, K. C. Dong, J. C. Li, M. P. Gordon, F. G. Reichertz, H. Kim, Y. Rho, Q. J. Wang, C. Y. Lin, C. P. Grigoropoulos, A. Javey, J. J. Urban, J. Yao, R. Levinson and J. Q. Wu, *Science*, 2021, **374**, 1504.

33 S. H. Fan and W. Li, *Nat. Photonics*, 2022, **16**, 182–190.

34 T. Wang, Y. Wu, L. Shi, X. H. Hu, M. Chen and L. M. Wu, *Nat. Commun.*, 2021, **12**, 11.

35 J. N. Munday, *Joule*, 2019, **3**, 2057–2060.

This journal is © The Royal Society of Chemistry 2025